Research Article

Shahroz Saleem, Abdullah Hasan Jabbar, Muhammad Hasnain Jameel*, Azka Rehman, Zahraa Hashim Kareem, Ali Hashim Abbas, Zunaira Ghaffar, Saba Abdul Razzaq, Rami Adel Pashameah, Eman Alzahrani, Eng-Poh Ng, and Salit Mohd Sapuan

Enhancement in structural, morphological, and optical properties of copper oxide for optoelectronic device applications

https://doi.org/10.1515/ntrev-2022-0473 received April 23, 2022; accepted June 27, 2022

Abstract: In this study, copper oxide (CuO) specimens were successfully prepared by the hydrothermal process at altered calcination temperatures; 350, 450, and 550°C. The synthesized samples were analyzed through X-ray powder diffraction (XRD), scanning electron microscope (SEM), Raman, Fourier-transform infrared spectroscopy (FTIR), and UV-Vis spectroscopy to analyze the impact of

* Corresponding author: Muhammad Hasnain Jameel, Shaanxi Key Laboratory for Theoretical Physics Frontiers, Institute of Modern Physics, Northwest University, Xi'an 710069, China; Department of Physics, Khwaja Fareed University of Engineering & Information Technology Rahim Yar Khan, 64200, Pakistan,

e-mail: mhasnainjamil@gmail.com

Shahroz Saleem: Shaanxi Key Laboratory for Advanced Energy Devices and Shaanxi Engineering Lab for Advanced Energy Technology, Xi'an 710119, China

Abdullah Hasan Jabbar: Optical Department, College of Medical and Health Technology, Sawa University, Ministry of Higher Education and Scientific Research, Al-Muthanaa, Samawah, Iraq

Azka Rehman: Department of Physics, Khwaja Fareed University of Engineering & Information Technology Rahim Yar Khan, 64200, Pakistan

Zahraa Hashim Kareem: Medical Instrumentation Techniques Engineering Department, Al-Mustaqbal University College, Babylon, Iraq

Ali Hashim Abbas: College of Information Technology, Imam Ja'afar Al-Sadiq University, Al-Muthanna 66002, Iraq

Zunaira Ghaffar, Saba Abdul Razzaq: Department of Physics, University of Agriculture, Faisalabad, 38040, Pakistan Rami Adel Pashameah: Department of Chemistry, Faculty of Applied Science, Umm Al-Qura University, Makkah 24230, Saudi Arabia Eman Alzahrani: Department of Chemistry, College of Science, Taif University, P.O. Box 11099, Taif 21944, Saudi Arabia

Eng-Poh Ng: School of Chemical Sciences, Universiti Sains Malaysia, 11800 USM, Malaysia.

Salit Mohd Sapuan: Department of Mechanical and Manufacturing Engineering, Faculty of Engineering, Universiti Putra Malaysia, Serdang 43400, Selangor, Malaysia

calcination temperature on the structural, morphological, vibration spectra, functional group, and optical properties of CuO for optoelectronic device applications. XRD confirms the pure single-phase monoclinic structure of synthesized samples with no impurity phases and has good crystallinity with the development in calcination temperature. The average crystalline size, lattice constant, and porosity were found in the range of 3.98-5.06 nm; a = 3.4357 Å, b = 3.9902 Å, c = 4.8977 Å - a = 3.0573 Å, $b = 3.9573 \,\text{Å}, c = 4.6892 \,\text{Å}; \text{ and } 3.37-1.03\%, \text{ respectively.}$ SEM exhibited a variation in morphology by increasing calcination temperature. Raman spectra revealed that the CuO sample calcinated at 550°C with a stone-like shape having a large grain size of 3.25 µm exhibited that Raman peak intensity and the multiphonon band became stronger and sharper and exhibited higher intensity compared to the samples calcinated at 350 and 450°C. FTIR spectra confirmed that these synthesized specimens exhibited the peaks associated with the typical stretching vibrations of the Cu-O bond between 400 and 500 cm⁻¹ exhibiting the formation of CuO. The energy bandgap was slightly reduced from 1.61 to 1.43 eV with the increase in the calcination temperature. The optical studies revealed that the calcination temperature of 550°C improves the optical properties of CuO by tuning its optical bandgap. The modified structural, morphological, and optical characteristics of the prepared CuO samples make them an appropriate candidate for optoelectronic device applications.

Keywords: copper oxide, XRD, Raman, SEM, FTIR, UV, optoelectronic devices

1 Introduction

During the past decade, there has been gained significant consideration in the progress of several electronic devices including solar cells, gas sensors, magnetic readers, photodetectors, catalysis, nonvolatile memory devices, and so on [1]. Optoelectronic devices are such important devices that can be applied in energy storage, information storage media, detection, and source of light. These devices can be a part of many applications, such as automatic access control systems, military services, and medical equipment [2]. Optoelectronic devices based on SnO₂ [3], CeO₂ [4], ZnO [5], Ga₂O₃ [6], and Fe₂O₃ [7] have been studied in detail. But, these 1D nanoparticle (NP)-based optoelectronic devices can be identified only by either visible or ultraviolet light due to their relatively largest bandgap.

Metal oxide semiconductors have been important materials in the area of materials science in the current decade. Semiconductors with a low bandgap, such as SiC, PbS, and copper oxide (CuO) due to their quantum confinement effect, higher surface-volume ratio, and some exceptional physical and chemical characteristics, have all been examined in detail for electrical and optoelectronic device applications [8]. Compared to inorganic semiconductor materials, metal oxide semiconductors are environmental friendly, show high mobility, are chemically and thermally stable, are inexpensive, are compatible, , and can be easily processed with semiconductors and metals. In the class of metal oxide semiconductors, CuO is a well-known p-type semiconductor material exhibiting the smallest direct energy bandgap of 1.3-2.1 eV at room temperature and can act as a promising material for optoelectronic devices, and hence, CuO is widely used for several optoelectronic device productions [9]. The CuO semiconductor is a kind of metal oxide that has been deliberated for several causes including higher theoretical capacity, safety, environmentally friendly, radiation resistance, chemical durability, nontoxicity, and also some exceptional characteristics like the optical and electronic characteristics. Furthermore, Cu can be converted into both Cu₂O and CuO based on the several distinct structures, oxidative environments, and the different morphologies [10,11]. Work about CuObased optoelectronic has not been extensively deliberated.

Numerous techniques are applied to fabricate CuO, such as sol-gel [12], pyrolysis [13], magnetron sputtering [14], hydrothermal [15], thermal oxidation [16], and co-precipitation [17]. Among these synthesis methods, hydrothermal is a well-known fast and facile production method to fabricate CuO due to its well-defined size and shape, scalable fabrication, and easy manipulation. However, the hydrothermal method is very rarely applied for the synthesis of nanomaterials. The current literature explains the hydrothermal production of CuO for optoelectronic device applications.

CuO also has some disadvantages, such as good photo response at a low bandgap than with a large bandgap, which limits its applications. CuO demonstrated a reduction in photo response with the particle size reduction due to the quantum confinement effect. In recent years, there was limited work described for improving the morphological, optical, and structural characteristics of CuO for optoelectronic devices. Jana et al. described that CuO NPs possess the energy bandgap reduction in the range of 1.63-1.34 eV with particle size enhancement. At this bandgap, these nanostructures showed good photo response for CuO-based devices [18]. Al-Amri et al. produced Ni-doped CuO NPs when the content of Ni dopant was increased, which caused to enhance the energy bandgap between 2.73 and 3.80 eV and reduce the particle size, and consequently, the smallest energy bandgap CuO NPs demonstrated good photo response for the optoelectronic devices compared with larger bandgap CuO-based optoelectronic devices [19]. Abd-Elnaiem et al. reported the synthesis of CuO nanowires by anodization of copper foams, which as a catalyst found to be useful in developing the photocatalytic efficiency of organic dye decomposition [20]. Giziński et al. reported the synthesis of CuO that was applied as a catalyst in the photoelechemical and electrochemical reactions, as this is a promising candidate as the electrode for nonenzymatic glucose sensors [21].

In this study, we produced CuO samples and performed their calcination at different temperatures such as 350, 450, and 550°C. In adddition, we demonstrated the impact of calcination temperatures on the morphology, optical, and structural characteristics, and vibrational mode of produced CuO. By varying the calcination temperatures, the particle size, average crystalline size, and Raman spectra were enhanced, while the porosity, agglomeration, and bandgap were reduced. As a result, the photo response of CuO-based optoelectronic devices was increased with the reduction in the wide bandgap at the highest temperature. Analyses of the produced samples were performed by using scanning electron microscope (SEM); Fourier-transform infrared spectroscopy (FTIR), UV-vis spectroscopy, Raman spectroscopy, and powder X-ray powder diffraction (XRD) techniques for analyzing their characteristics in detail.

2 Experimental details

CuO was produced through hydrothermal synthesis by considering sodium hydroxide (NaOH) and copper sulfate (CuSO $_4$ ·2H $_2$ O) as initial chemical materials, and

double-distilled water was used to dissolve these chemicals in it. CuSO₄·2H₂O is highly soluble in water with solubility value of 1.055 molar, and its solubility increases with an increase in heat. CuSO₄ 2H₂O was used as a source of Cu. A stoichiometric amount of CuSO₄·2H₂O (0.2 M) and NaOH (0.4 M) were separately dissolved into 150 mL double-distilled water with continuous stirring on an electronic stirrer. After complete mixing, 50 mL of 5-M NaOH was placed into this solution to maintain pH at 9 during the complete chemical reaction. This chemical solution was placed in a Teflon-lined sealed stainless steel autoclave at a constant temperature of 200°C for 6 h in autogenerous pressure. This product was then placed at room temperature and cooled. The obtained product was kept in the furnace at the calcination temperature of 350°C for 1 h. The black product was centrifuged, washed completely with double distilled water many times, washed three times with ethanol, and thoroughly dried in air at room temperature. This material was then ground, and finally, the fine material in the black powder form was obtained, which is known as CuO. Similarly, two more specimens were fabricated at the calcination temperature of 450 and 550°C, respectively.

The XRD-determined data were collected after Cu K α radiation in the peak position (2 θ) range of 20–60°, while the scanning step size is 0.05° and the rate is 6° min⁻¹. The SEM (JEOL Model JSM-6390LV) with an operating voltage 20 KV was used to examine the CuO morphology. The Varian, Cary 5000 spectrophotometer was used to examine the UV-Vis spectrum of CuO samples between 300 and 800 nm. The molecular structure of the prepared products was confirmed by Thermo Nicolet, Avatar370 FT-IR spectrometer. Raman spectroscopy was used to characterize the CuO samples to confirm their atomic molecular arrangements.

2.1 Structural analysis

Figure 1 shows the XRD peaks of the fabricated CuO specimens. These peaks are similar to JCPDS 5-661 and showed the monoclinic structure, confirming its pure phase with lattice constants (a=3.4357, b=3.9902, and c=4.8977), (a=3.1903, b=3.9789, and c=4.6892), for the specimens calcined at 350, 450, and 550°C, respectively. The most intense and characteristic peak among all XRD patterns corresponds to the reflecting plane (111), which shows the formation of a single-phase monoclinic structure. With the enhancement in calcination

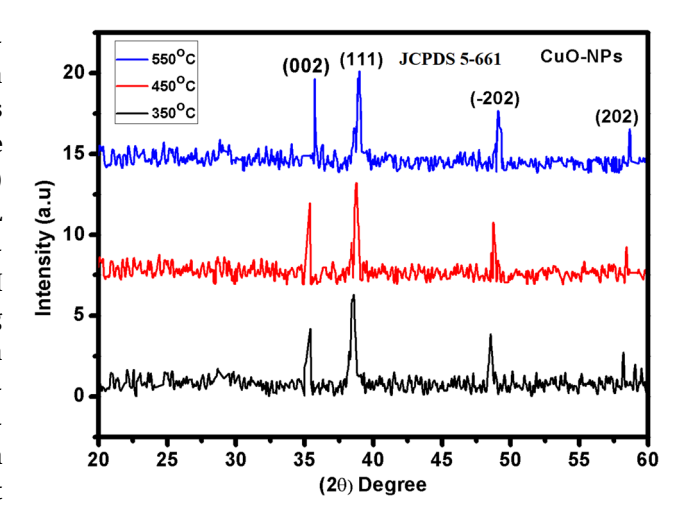


Figure 1: XRD diagram of CuO samples calcinated at 350, 450, and 550°C.

temperature, the full width at half maximum (FWHM) was slightly decreased, and the intensity of XRD peaks slightly improved due to crystallinity and crystallite size increased. XRD analysis confirmed the nonexistence of impurity phases that represents the phase purity of CuO samples. Table 1 presents that the crystalline size is enhanced by about 3.98-5.06 nm with the increase of the calcination temperature from 300 to 500°C. In the case of the smallest crystalline size, lower calcination temperature may cause slow nucleation and growth process, which prevents grain from growing during the time scale of the experiment; therefore, crystalline size is smaller at the calcination temperature of 350°C. But when calcination temperature increases to 550°C, the growth and nucleation process are almost simultaneously fast vielding lower monodispersity and larger crystalline size. The sample with a smaller grain size has a larger surface area, which was reduced with the increase in the crystalline size at the higher calcination temperature of 550°C. This specific surface area with the increasing calcination temperature can be associated with the agglomeration of the grains, and as a result, the densification process may be deliberated [22].

The Debye–Scherrer formula was applied for the calculation of the average crystalline size from the peak (111) [23].

$$D = \frac{K\lambda}{\beta \cos \Theta},\tag{1}$$

where "K" is the shape factor, which has a constant value of 0.94, λ is the wavelength of falling X-ray radiation, and " β " is the full width at half the maximum value of the diffraction angle θ . The specific surface area can be calculated by the following formula [24]:

2830 — Shahroz Saleem et al. DE GRUYTER

Table 1: XRD data of different parameters of CuO samples calcinated at 350, 450, and 550°C

Calcination temperature (°C)	Crystalline size (nm)	d- Spacing (Å)	Lattice constant (Å)	Lattice volume (Å)		Bulk density (g/cm³)	Porosity (%)	X-ray density Bulk density Porosity (%) Williamson–Hall (g/cm 3) analysis (ε)	Dislocation density (<i>ō</i>)
350°C	3.98	2.4846	3.4357 3.9902 4.8977 58.1477	7 58.1477	1.07	1.03	3.37	5.03×10^{-3}	6.31×10^{-2}
450°C	4.11	2.4779	3.1903 3.9789 4.774	4.7744 52.4860	1.12	1.10	1.78	4.45×10^{-3}	5.91×10^{-2}
550°C	5.06	2.4648	3.0573 3.9573 4.6892 49.1322	2 49.1322	1.94	1.92	1.03	3.18×10^{-3}	3.90×10^{-2}

$$S = 6/D\rho. (2)$$

The constant 6 is known as the form factor of spherical particles; "D" is the crystallite size, while " ρ " is X-ray density. The calculated values of specific surface areas are 1.4089, 1.3034, and 0.6112 m²/kg.

The Bragg formula $\lambda = 2d \sin \theta$ was used to determine the *d*-spacing values among atomic layers. The lattice constants value *a*, *b*, and *c* were calculated by equation (3). The lattice geometry formula was used to determine the primary unit cell volumes (V) [25].

$$V = abc \sin \beta. \tag{3}$$

The experimentally calculated values of *d*-spacing and lattice constant are given in Table 1. The values of lattice parameters have been calculated by using the miller indices and determined d-spacing values of characteristic peak (111) of three samples. The shrinkage of the lattice constant was caused by the increase in temperature; therefore, the lattice constant decrease from which attributed to the heat coupling due to calcination temperature, at the highest temperature, d-spacing between atoms was largest due to which heat coupling in the sample allowing the copper atoms to diffuse towards the tetrahedral site, therefore lattice constant was higher. In the case of the smallest lattice constant, d-spacing between atoms was the smallest due to which the copper atoms by heat coupling could not much be allowed to diffuse toward the tetrahedral site; therefore, the lattice constant was reduced.

The X-ray density (ρ_{XRD}) can be calculated by the following relation [26]:

$$\rho_{XRD} = \frac{Z M}{N_{\Delta} V}, \tag{4}$$

where "Z" is some molecules per unit cell, "M" is the molecular weight, " N_A " is Avogadro's number, and "V" is the monoclinic unit cell volume, and its value from equation (4) is substituted in equation (5):

$$\rho_{XRD} = \frac{8A}{Nabc \sin \beta},\tag{5}$$

where M is the molecular weight of the particular oxide and $abc \sin \beta$ is the volume of the monoclinic unit cell. X-ray density (ρ_{XRD}) was enlarged by about 1.07–1.96 g/cm³ by the growth temperature of about 350–550°C. The growth in molecular weight of the sample became the main cause behind the growth of X-ray density (ρ_{XRD}).

The Archimedes principle was used to determine the bulk density (ρ_{β}) of all samples, which is presented in equation (6). At the calcination temperature from 350 to 550°C, the bulk density was enhanced by about

1.03–1.92 g/cm³. The small bulk density was associated with the pore creation and increased during the synthesis mechanism, which was enhanced due to the growth of the temperature, and as a result, the bulk density was enhanced [27].

$$\rho_{\rm B} = \frac{m}{V}.\tag{6}$$

The porosity has been determined through equation (7) [28]. The porosity was reduced from 3.37 to 1.03% with the development in the temperature of about 350–550°C. In this mathematical form, (ρ_{β}) and (ρ_{x}) are bulk density and X-ray density, respectively, which are given in Table 1.

Porosity =
$$\left(1 - \frac{\rho_{\rm B}}{\rho_{\rm x}}\right) \times 100\%$$
. (7)

The dislocation density, described as the length of dislocation lines per unit volume of the crystal, can be determined by equation (8). It is the measure of the number of dislocations present in the content of the material. Dislocations are the irregularity or crystallographic defect in a crystal that arises from the lattice mismatch from another part of that crystal. This can be determined by the following formula [29]:

$$\delta = 1/D^2. \tag{8}$$

As the temperature increases, FWHM begins to decrease and the peak intensity increases, which shows that the crystalline size decreases because of the influence of the strain factor due to fabrication; therefore, dislocation density is reduced. The increasing calcination temperature produces the least crystallographic defects in the crystal of synthesized material, which reveals the better crystallinity of that material.

2.2 Microstrain

The microstrain produced in the lattice by the altered calcination temperature on CuO specimens was estimated by the W–H method of analysis; the crystalline size was also calculated from this method by using equation 9. The distortion and microstrain or crystal imperfection are mathematically expressed as $\varepsilon = \beta_s/4 \tan \theta$, which arise by microstrain (ε) and strain-induced broadening. In the W–H method, crystalline size changes with $\tan \theta$, while in the case of Scherrer's equation, crystalline size varies with $1/\cos \theta$.

Grain size broadening and broadening are used to obtain the total integral breadth of the Bragg peak, which are expressed as follows [30]:

$$B_{hkl} = \beta_D + \beta_S,$$

$$B_{hkl} = k\lambda/D \cos \theta + 4\varepsilon \tan \theta,$$

$$B_{hkl}(\cos \theta) = k\lambda/D + (4\varepsilon \sin \theta).$$
 (9)

In this method, the microstrain can be estimated by the slope of the graph plotted between " $4 \sin \theta$ " versus " $\beta_{hkl}\cos\theta$ ", while the crystalline size can be estimated from the y-intercept, as shown in Figure 2. From this method, it can be seen that the crystalline sizes of CuO samples calcinated at 350, 450, and 550°C were 7.30, 9.51, and 12.60 nm, respectively. Both of these approaches provided nearly comparable consequences, but the Williamson-Hall plot method was giving some large crystalline size. This large size can be due to the existence of changed geometries of grains and microstrain in the crystal lattice of samples. As the calcination temperature increases from 350 to 550°C, the microstrain decreases from 5.03×10^{-3} to 3.18×10^{-3} . An increase in the calcination temperature of CuO samples becomes a reason for the increasing crystalline size and enlarging crystallite boundary movement, and thus increasing the grain development. Consequently, the disorder effect was reduced, which became a cause of decreasing broadening and enhancing the intensity of XRD peaks. Therefore, the microstrain and dislocation density reduce because of the decrease in lattice defects with grain boundaries on increasing the calcination temperature of the CuO sample. From the examined data, the microstrain in CuO crystallines may arise from excess boundaries by dislocations. It is noted that the fitting is so bad, and this bad fitting may be due to the noise signals produced during the growth and nucleation process caused by the calcination temperature.

2.3 Morphological analysis

The specimens were observed by SEM to analyze their size and morphology. The SEM images of the prepared CuO samples are illustrated in Figure 3. The grains shown in Figure 3(a) are irregular in shape, that shown in Figure 3(b) are in a random shape, and that shown in Figure 3(c) are in a stone-like shape. For the samples calcinated at 350, 450, and 550°C, the size of grains analyzed in SEM pictures is within the range of $1.06-3.25\,\mu m$.

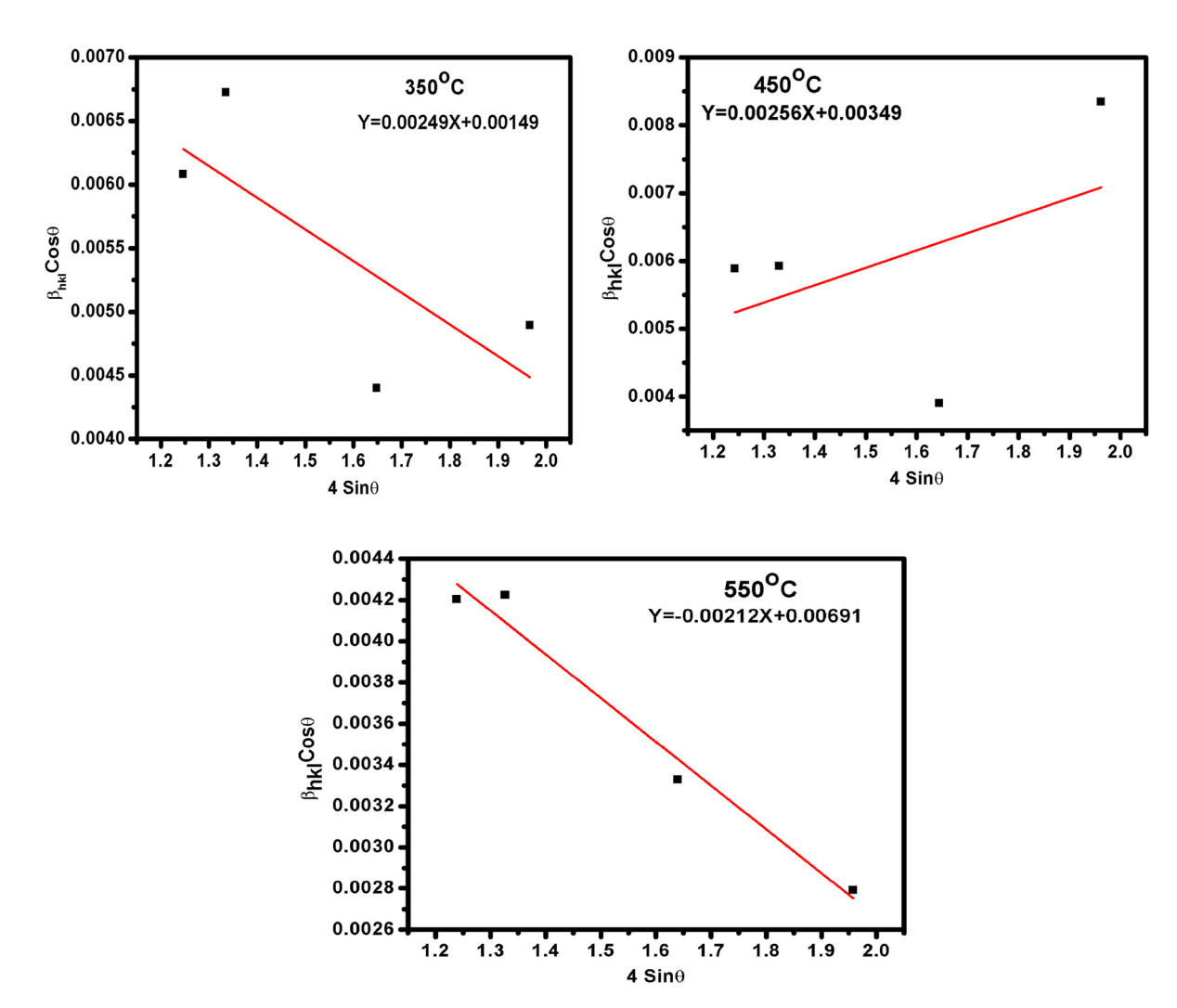


Figure 2: Williamson-Hall plots of CuO samples calcinated at calcination temperatures of 350, 450, and 550°C.

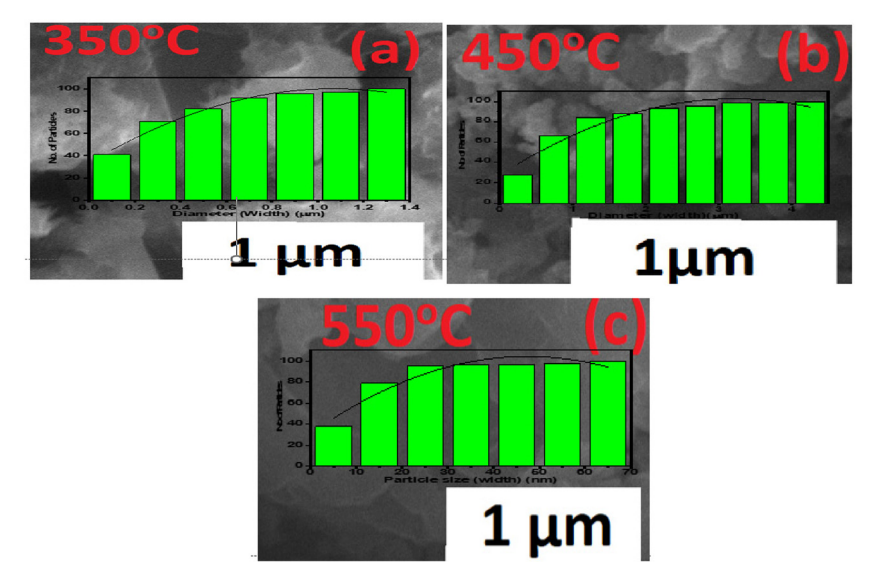


Figure 3: SEM pictures of CuO samples calcinated at (a) 350, (b) 450, and (c) 550°C.

The agglomeration among grains was reduced with the temperature growth. Due to the high surface charge and high magnetization among grains, agglomeration occurred in the Ostwald ripening process. The lower calcination temperature of 350°C produces a large number of cores and decreases the rate of the nucleation process, which prevents the grains from growing and causes the agglomeration due to the high intense collapse of bubbles, and the grain size was 1.06 µm. When the temperature increased up to 550°C, a small number of cores formed among grains because of which small agglomeration takes place due to less intense collapse of bubbles. Therefore, when the temperature was enlarged from 300 up to 500°C, the rate of the nucleation process increases because of the existence of charges at the surface of the grains and then agglomeration decreases due to a reduction in the number of cores, and consequently, grains grow up to 3.25 µm and crystallinity also increases. In other words, the space between the grains is slightly increased by the increase in calcination temperature, which reduces the agglomeration of grains. The grains exhibit irregular morphology due to the agglomeration of primary grains, which were minimally increased with the increase in the calcination temperature. The grain size grows with the growth in the calcination temperature, and the consistency of size and shape of CuO was detected. Further, with the increase in the size of grains, the bandgap decreases, due to which electronic conduction between valance and conduction band increased, and hence, the working capability of a device increased.

2.4 Raman analysis

Raman spectroscopy, which is a very sensitive probe to the vibrations of the material and its local atomic arrangements, has been usually employed for the examination of the microstructural nature of the materials. Raman scattering also gives important details about the bonds and structures of materials [31] and is also used to identify the presence of unintended phases such as Cu (OH)₂, Cu₂O, and material crystallinity. Since there are two molecules in each primitive cell of the CuO with space group C_{2h}^6 , its Raman active normal modes at central zones of copper oxide molecules are at $\Gamma_{RA} = 4A_u + 5Bu + A_g + 2B_g$. Raman spectra of three CuO samples are illustrated in Figure 4, and it can be seen that Raman spectra have two main one-phonon modes. The peak

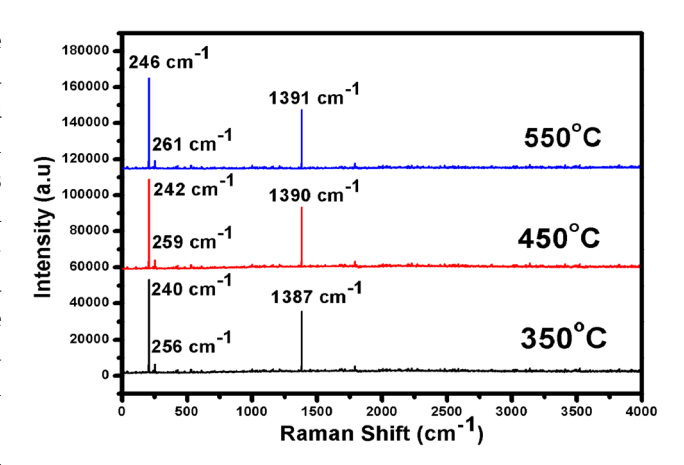


Figure 4: Raman spectra of the prepared CuO samples calcinated at 350, 450, and 550°C.

assignments at 240, 242, and 246 cm⁻¹ are related to the $A_{\rm g}$ mode of vibration of samples calcinated at 350, 450, and 550°C, respectively, while the peaks at 256, 259, and 261 cm⁻¹ are assigned to B_g mode of vibration of samples calcinated at 350, 450, 550°C, respectively. These peaks assignments are nearly equal to the reported data in the previous study [32]. Maximum physical characteristics of any material are produced due to the interactions among the vibration modes of molecules. The oxygen atoms only move with a displacement in the b-direction for A_g and perpendicular to the b-axis for B_g Raman modes. Irwin and Wei reported that crystal defects reduce with the increase in the crystalline size of NPs due to the smaller surface/ volume ratio, and these crystal defects can contribute to Raman spectra as all three of the Raman modes in CuO are assigned to vibrations of oxygen atom [33].

It is noted that the multiphonon Raman band peakes of CuO specimens which are calcinated at different temperatures of 350, 450, and 550°C that presented at 1,387, 1,390, and 1,391 cm⁻¹. In particular, the multiphonon band $2B_g$ in CuO was suggested to be the stretching vibration in the x^2-y^2 plane, induced by the electronic density deviation in this layer. The shift of these peaks toward higher wavenumbers (redshift) and appropriately low value of FWHM ascertains the CuO NPs. The phonon confinement effect is utilized to describe the redshift in materials. The production of redshift and lowering or decreasing broadening of Raman modes may be due to the reduction of the agglomeration state. As the Raman peaks move toward high wavenumbers, it means that CuO can be an excellent material for optoelectronic device applications.

The intensity of the multiphonon Raman peak is very weak in comparison with one phonon band and changes

with the size and morphology of fabricated CuO samples. It has been described that the multiphonon band of the as-produced CuO grains with stone-like morphology and 3.25 µm particles possess greater intensity than that of CuO grains with random morphology and 3.21 µm, which in turn is greater than that of CuO grains with irregular morphology and 1.06 µm grain size. Anisotropy of different CuO NPs is utilized to describe the dissimilarity in the Raman intensity of different morphologies. The electronic movement among the x-y plane becomes substantial in the x-y plane and changes the intensity of $2B_{\sigma}$ mode in the irregular-, random- and stone-like grains. Another description for the change in the Raman intensity of this mode is the phonon-plasmon coupling because of the higher local density of anisotropic carriers CuO grains. A crystallinity effect and finite size of these grains are revealed by the change in the multiphonon intensity.

2.5 Chemical composition analysis

Fourier transform-infrared spectroscopy in the transmission mode was utilized to generate the spectra for obtaining the information about compounds present on CuO samples and to obtain sufficient information about the molecular information of CuO samples, which were produced at the calcination temperatures of 350, 450, and 550°C. The functional group spectra were analyzed between 400 and 4,000 cm⁻¹. Peaks found at 446, 452, 469 cm⁻¹ for three samples can be related to the highfrequency Au mode of CuO; these high-frequency modes are related to the typical stretching vibrations of Cu-O bond in the monoclinic structure of three CuO samples, which confirmed the formation of CuO as shown in Figure 5. These peaks were detected from Cu-O stretching along the (202) direction [34]. The small bands found between 2,100 and 2,200 cm $^{-1}$ are assigned to 0=C=0 stretching vibrations. The region between 3,600-3,800 cm⁻¹ contained the strong broadband peaks of O-H vibrational stretching surface of the hydroxyl groups of adsorbed water molecules. The IR band found between 1,000 and 1,100 cm⁻¹ can be assigned to C-OH stretching and O-H bending vibration, exhibiting the presence of a large number of hydroxyl groups [35]. The peaks noticed between the regions of 2,900 and 3,000 cm⁻¹ are attributed to C-H stretching vibrations of different molecules as presented in Table 2 [36]. Furthermore, no impurities were detected. The IR spectra confirmed the pure monoclinic crystal structure of the prepared CuO samples.

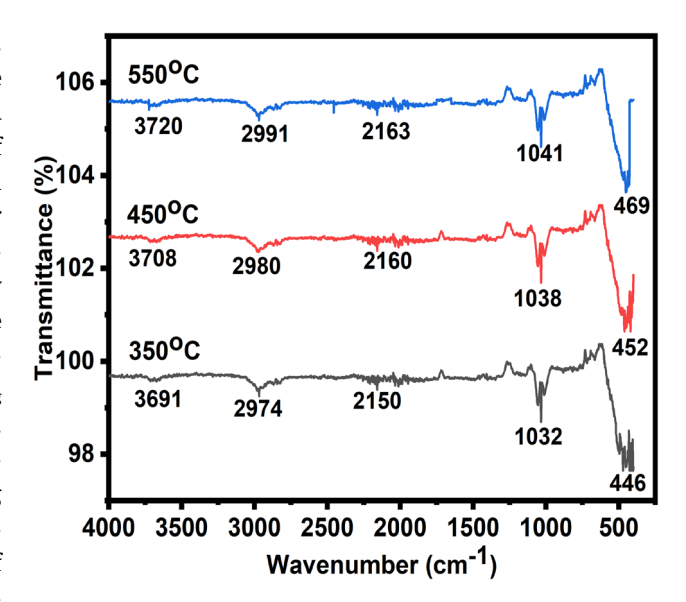


Figure 5: FTIR spectra of CuO samples calcinated at 350, 450, and 550°C.

Table 2: FTIR spectra with possible assignments for CuO samples calcinated at 350, 450, and 550°C

Frequency (cm ⁻¹)			Possible assignment
350°C	450°C	550°C	
446	452	469	Cu-O stretching vibration
1,032	1,038	1,042	C-OH stretching and OH bending vibration
2,150	2,160	2,163	0=C=0
2,974	2,980	2,991	C-H stretching vibrations
3,691	3,708	3,720	O-H stretching vibrations

2.6 Optical studies

Ultra-visible (UV) spectra were utilized to examine the optical characteristics of CuO samples. The UV-vis absorbance spectra were estimated for three CuO samples in the range of 300–800 nm, and the energy bandgap is illustrated in Figure 6. The values of the energy bandgap for three samples are determined by the Tauc relation:

$$\alpha h \nu = A(h \nu - E_g)^n, \tag{10}$$

where "v" is the frequency of the light source, " α " is an absorption coefficient, "A" is constant (independent of n), "h' is Plank's constant, and "n" is the exponent, which is governed by the quantum selection rules.

Figure 6 shows the absorption edges for the CuO samples at blue shift regions 436, 543, and 549 nm, which correspond to the wide energy bandgap of 1.61, 1.53, and 1.43 eV, respectively. There is an additional fact that

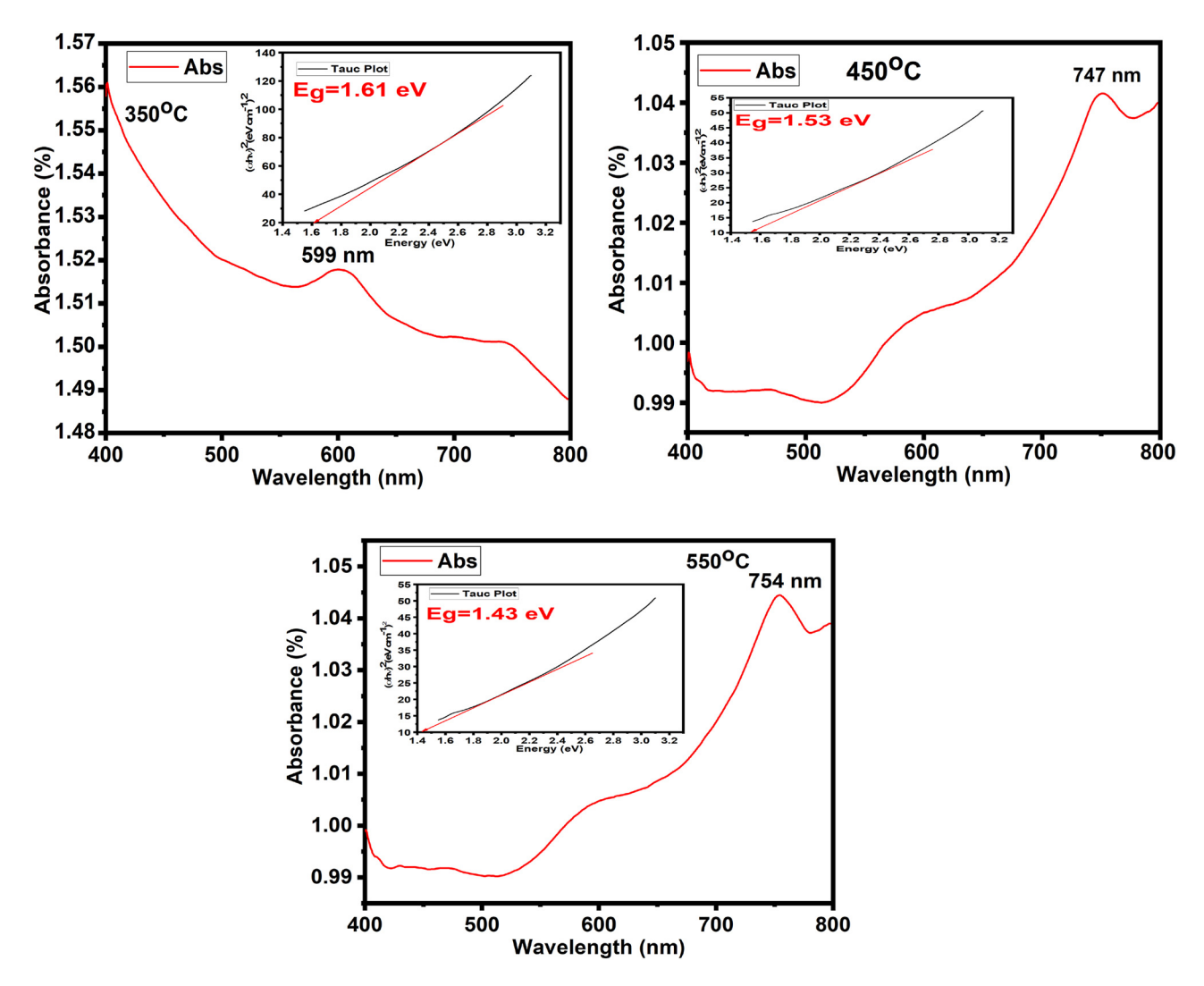


Figure 6: UV absorbance and optical bandgap of CuO samples calcined at 350, 450, and 550°C.

absorbance is reduced with the wavelength enhancement, which revealed the existence of an energy bandgap in these three CuO samples.

The optical properties of the synthesized CuO samples were analyzed for the determination of the electronic transition type and bandgap. When a semiconductor absorbs the energy, photons have energy more than its bandgap, and then move the electrons from the valance bandgap to the conduction band, and as a result, the wavelength absorbance capacity semiconductor improved consistently to the energy bandgap. A relation between absorption coefficient and falling photon's energy depends on the electronic transition type. When the electron momentum is conserved, the transition is directly due to conserved electron momentum. However in indirect bandgap structure, during the electronic transition momentum and exchange of photons was not conserved.

To our knowledge, when any material absorbs light, then electron goes from valence to the conduction band, and their energy levels are quantized by free electrons [37]. In our research work, there are a few features such as defects, for example, vacancies in CuO NPs (e.g., Cu¹⁺ and O vacancies) and quantum size effect, which reduced with the decrease in the energy bandgap due to the increasing calcination temperature [19,37–39].

CuO has the standard bandgap of 1.20 eV. In our work, the synthesized samples have a lightly more bandgap of 1.61, 1.53, and 1.43 eV, at the calcination temperature of 350, 450, and 550°C, respectively, as shown in Table 3. The defect that exists behind the wide bandgap is the slight high energy of conduction band minimum (CBM), which is nearly equal to the reported bandgap in the reports [36], and this high bandgap causes the CuO sample to show the slightly high resistivity and slightly low conductivity. But when the calcination

Table 3: The bandgap for CuO samples calcinated at 350, 450, and 550°C

Samples	Absorption wavelength (nm)	Bandgap (eV)
350°C	599	1.61
450°C	747	1.53
550°C	754	1.43

temperature increased to 550°C, slightly high energy of CBM becomes low, and hence, the bandgap reduced up to 1.43 eV. So resistivity is reduced and conductivity enhanced. In the present case, CuO samples exhibit their electronic properties in the range of semiconductor materials. The optoelectronic devices such as power switching instruments can be worked at calculated bandgap 1.61 eV, 1.53 eV, 1.43 eV with different calcinated temperatures at 350, 450, and 550°C moreover it can also work at slightly higher temperature. These CuO semiconductor materials are beneficial at larger wavelengths compared to other low-bandgap CuO semiconductor materials. The required temperature to operate such a bandgap CuO-based optoelectronic device would be reduced with the reduction in this bandgap of CuO, and hopefully, this bandgap will reduce with a further increase in the calcination temperature. In such a way, the CuO with reducing bandgap would be shown as a good photoresponse for optoelectronic devices compared to larger bandgap CuO.

3 Conclusion

In this study, a hydrothermal method was used for the synthesis of CuO samples to analyze the impact of calcination temperatures on the structural, morphological, vibration mode, and optical properties. XRD showed that the prepared products have a pure monoclinic phase and crystalline nature. A single-phase monoclinic structure of CuO having an average crystallite size of 3.98-5.06 nm was confirmed by XRD without the impurity phase. This increase in the crystallite size was due to the increase in nucleation and growth process with the increase in calcination temperature. *d*-spacing, lattice constant, unit cell volume, porosity, dislocation density, and microstrain were decreased by increasing the calcination temperature. A small decrement in dislocation density and microstrain in CuO samples was noted due to an increase in the crystalline size at the highest calcination temperature of 550°C, showing the least crystallographic defect and

lattice defect in a crystal, which confirmed its better crystallinity and structural improvement. SEM images revealed that agglomeration was decreased by the increasing calcination temperature, which was responsible for the decrease in porosity. Raman spectra revealed that the CuO sample calcinated at 550°C with a stone-like shape having a large grain size of 3.25 µm exhibited that Raman peaks intensity and the multiphonon band became stronger and sharper and exhibited higher intensity than that of calcination at lower temperatures. FTIR spectra confirmed that these synthesized specimens exhibited the peaks associated with the typical stretching vibrations of Cu-O bond in the range of 400-500 cm⁻¹, which revealed the formation of CuO. The bandgap energy was decreased from 1.61 to 1.43 eV due to the quantum confinement effect by increasing calcination temperature, which is in good agreement with XRD results. These obtained consequences suggested that increasing the calcination temperature improves the structural, morphological, vibrational model, and optical properties of CuO and makes them the best candidate for the development of those optoelectronic devices, which are constructed on the basis of such low bandgap CuO materials and can only operate at the low temperature. Such optoelectronic devices cannot operate at a higher temperature because there may be a high probability of burning or damaging of device. However, further enhancements in the calcination temperature for CuO samples may be employed to study in detail its effect on the structural, morphological, vibrational model, and optical properties of CuO.

Acknowledgments: The authors would like to thank the Deanship of Scientific Research at Umm Al-Qura University for supporting this work by Grant Code: (22UQU4320141DSR25). This work was supported by the National Natural Science Foundation of China under Grants (Nos. 51872227 and 51572219).

Funding information: This work was supported by Grant Code: (22UQU4320141DSR25) of the Deanship of Scientific Research at Umm Al-Qura University. This work was supported by the National Natural Science Foundation of China under Grants (Nos. 51872227 and 51572219).

Author contributions: All authors have accepted responsibility for the entire content of this manuscript and approved its submission.

Conflict of interest: The authors state no conflict of interest.

Data availability statement: The datasets generated during and/or analyzed during the current study are available from the corresponding author on reasonable request.

References

- Luo LB, Wang XH, Xie C, Li ZJ, Lu R, Yang XB, et al. One-dimensional CuO nanowire: synthesis, electrical, and optoelectronic devices application. Nanoscale Res Lett. 2014:9(1):1-8.
- [2] Dutta NK, Zhang X. Optoelectronic devices. Singapore: World Scientific; 2018.
- Hadi A, Hashim A, Al-Khafaji Y. Structural, optical and electrical properties of PVA/PEO/SnO2 new nanocomposites for flexible devices. Trans Electr ElectrMater. 2020;21(3):283-92.
- Aziz SB, Dannoun E, Tahir DA, Hussen SA, Abdulwahid RT, Nofal MM, et al. Synthesis of PVA/CeO2 based nanocomposites with tuned refractive index and reduced absorption edge: Structural and optical studies. Materials. 2021;14(6):1570.
- Capper P, Kasap SO, Willoughby A. Zinc oxide materials for electronic and optoelectronic device applications. Hoboken, NJ: John Wiley & Sons; 2011.
- Xiao M, Dong K, Liang J, He J, Fang G. Enhanced photoresponse performance of Cu₂O-based graded heterojunction optoelectronic devices with Ga_2O_3 buffer layer. J Mater Chem C. 2022;10(14):5505-13.
- Veeralingam S, Borse PH, Badhulika S. 1D NiO-3D Fe₂O₃ mixed dimensional heterostructure for fast response flexible broadband photodetector. Nanotechnology. 2022;33(23):235201.
- Nesa M, Momin MA, Sharmin M, Bhuiyan AH. Structural, optical and electronic properties of CuO and Zn doped CuO: DFT based first-principles calculations. Chem Phys. 2020;528:110536.
- Tetseo M, Deb P, Daimary S, Chandra J. CuO nanowire based metal semiconductor metal infrared photodetector. Appl Phys A. 2021;127(5):1-6.
- [10] Noothongkaew S, Thumthan O, An KS. UV-Photodetectors based on CuO/ZnO nano-composites. Mater Lett. 2018;233:318-23.
- [11] Hussein HT, Mohammed MK, Kamel RI, Nayef UM. Improved sensing performance of porous silicon photodetector with CuO nanoparticles. Chem Pap. 2021;75(12):6257.
- [12] Arunkumar B, Jeyakumar SJ, Jothibas M. A sol-gel approach to the synthesis of CuO nanoparticles using Lantana camara leaf extract and their photo catalytic activity. Optik. 2019;183:698-705.
- [13] Chatragadda K, Vargeese AA. Synergistically catalysed pyrolysis of hydroxyl terminated polybutadiene binder in composite propellants and burn rate enhancement by free-standing CuO nanoparticles. Combust Flame. 2017;182:28-35.
- [14] Verma M, Kumar V, Katoch A. Sputtering based synthesis of CuO nanoparticles and their structural, thermal and optical studies. Mater Sci Semicond Process. 2018;76(November 2017):55-60.
- [15] Thangamani JG, Pasha SKK. Chemosphere Hydrothermal synthesis of copper (II) oxide-nanoparticles with highly

- enhanced BTEX gas sensing performance using chemiresistive sensor. Chemosphere. 2021;277(2):130237.
- [16] Kaur M, Muthe KP, Despande SK, Choudhury S, Singh JB. Growth and branching of CuO nanowires by thermal oxidation of copper. J Cryst Growth. 2006;289:670-5.
- [17] Anwar H, Naqvi SM, Abbas B, Shahid M, Iqbal M, Shahyar M, et al. Investigation of the effect of annealing temperature on structural, optical and antibacterial properties of copper oxide nanoparticles prepared by facile co-precipitation route. J Optoelectronic Biomed Mater. 2020;12(2):43-50.
- [18] Jana R, Dey A, Das M, Datta J, Das P, Ray PP. Improving performance of device made up of CuO nanoparticles synthesized by hydrothermal over the reflux method. Appl Surf Sci. 2018:452:155-64.
- [19] Al-Amri S, Ansari MS, Rafique S, Aldhahri M. Ni doped CuO nanoparticles: Structural and optical characterizations Ni doped CuO nanoparticles: Structural and optical characterizations. Curr Nanosci. 2015;11(2):191-7.
- [20] Abd-Elnaiem AM, Abdel-Rahim MA, Abdel-Latief AY, Mohamed AAR, Mojsilović K, Stępniowski WJ. Fabrication, characterization and photocatalytic activity of copper oxide nanowires formed by anodization of copper foams. Materials. 2021;14(17):5030.
- [21] Giziński D, Brudzisz A, Santos JS, Trivinho-Strixino F, Stępniowski WJ, Czujko T. Nanostructured anodic copper oxides as catalysts in electrochemical and photoelectrochemical reactions. Catalysts. 2020;10(11):1338.
- Kumar H, Srivastava RC, Negi P, Agrawal HM, Singh A. Effect of [22] sintering temperature on the structural properties of cobalt ferrite nanoparticles. Int J Mater Eng Innov. 2014;5(3):227-37.
- [23] Hasnain MJ, Ahmed S, Jiang ZY, Tahir MB, Akhtar MH, Saleem S, et al. First principal calculations to investigate structural, electronic, optical, and magnetic properties of Fe₃O₄ and Cd-doped Fe₂O₄. Comput Condens Matter. 2022;30(December 2021):e00629.
- [24] Torres A, Ruales C, Pulgarin C, Aimable A, Bowen P, Sarria V, et al. Innovative high-surface-area CuO pretreated cotton effective in bacterial inactivation under visible light. ACS Appl Mater Interfaces. 2010;2(9):2547-52.
- [25] Saleem S, Jameel MH, Akhtar N, Nazir N, Ali A, Zaman A, et al. Modification in structural, optical, morphological, and electrical properties of zinc oxide (ZnO) nanoparticles (NPs) by metal (Ni, Co) dopants for electronic device applications. Arab J Chem. 2022;15(1):103518.
- [26] Jameel MH, Agam MA, Hamzah MQ, Roslan MS, Rizvi SZH, Yabagi JA. Structural, optical and morphological properties of zinc -doped cobalt-ferrites $CoFe_2$ - $xZnxO_4$ (x = 0.1-0.5). Dig J Nanomater Bio-structures. 2021;16(2):399-408.
- [27] Jameel MH, Saleem S, Hashim M, Roslan MS, Somaily HHN, Hessin MM, et al. A comparative study on characterizations and synthesis of pure lead sul fi de (PbS) and Ag - doped PbS for photovoltaic applications. Nanotechnol Rev. 2021:1484-92.
- Navale YH, Navale ST, Stadler FJ, Ramgir NS, Debnath AK, [28] Gadkari SC, et al. Thermally evaporated copper oxide films: A view of annealing effect on physical and gas sensing properties. Ceram Int. 2017;43(9):7057-64.
- [29] Ali A, Jameel MH, Uddin S, Zaman A, Igbal Z, Gul Q, et al. The effect of Ca dopant on the electrical and dielectric properties of BaTi₄O₉ sintered ceramics. Materials. 2021;14:1-11.

- [30] Reddy KR. Green synthesis, morphological and optical studies of CuO nanoparticles. J Mol Struct. 2017;1150:553-7.
- [31] Tran TH, Nguyen VT. Copper oxide nanomaterials prepared by solution methods, some properties, and potential applications: A brief review. Int Sch Res Not. 2014;2014:1-14. doi: 10.1155/2014/856592.
- [32] Sundar S, Venkatachalam G, Kwon SJ. Biosynthesis of copper oxide (CuO) nanowires and their use for the electrochemical sensing of dopamine. Nanomaterials. 2018;8(10):823.
- [33] Siddiqui H, Qureshi MS, Haque FZ. Optik Surfactant assisted wet chemical synthesis of copper oxide (CuO) nanostructures and their spectroscopic analysis. Opt - Int J Light Electron Opt. 2016;127(5):2740-7.
- [34] Mary APA, Ansari AT, Subramanian R. Journal of king saud university – science sugarcane juice mediated synthesis of copper oxide nanoparticles, characterization and

- their antibacterial activity. J King Saud Univ Sci. 2019;31(4):1103-14.
- [35] Xu JF, Ji W, Shen ZX, Li WS, Tang SH, Ye XR, et al. Raman spectra of CuO nanocrystals. J Raman Spectrosc. 1999;415:413-5.
- [36] Katwal R, Kaur H, Sharma G, Naushad M, Pathania D. Electrochemical synthesized copper oxide nanoparticles for enhanced photocatalytic and antimicrobial activity. J Ind Eng Chem. 2015;31:173-84.
- [37] Vijayashree K, Rai KS, Demappa T. Synthesis of nanosized copper oxide by assimilating microwave radiation and its characterizations. Indian J Adv Chem Sci. 2016;1:6-9.
- [38] Yuan GQ, Jiang HF, Lin C, Liao SJ. Shape- and size-controlled electrochemical synthesis of cupric oxide nanocrystals. J Cryst Growth. 2007;303:400-6.
- [39] Ali MJM, Radhy MM, Ali EM. Synthesis and characterization of copper oxide nanoparticles and their application for solar cell. Mater Today Proc. 2021;60:917-21.